ACS Photonics

Article

pubs.acs.org/journal/apchd5

Effect of Intertip Coupling on the Plasmonic Behavior of Individual Multitipped Gold Nanoflower

Achyut Maity, Arpan Maiti, Pabitra Das,† Dulal Senapati, and Tapas Kumar Chini*

Saha Institute of Nuclear Physics, 1/AF Bidhannagar, Kolkata 700 064, India

Supporting Information

ABSTRACT: We report here, the first experimental realization on the selective excitation of two closely lying tips from the same spherical core of a multitipped gold nanoparticle with flower-like morphology. This gives strong multipeaked resonance in the near-infrared region of the far-field emission spectra showing a clear signature of tip to tip coupling. The cathodoluminescence (CL) technique in a scanning electron microscope (SEM) combined with finite-difference time-domain (FDTD) simulation has helped us to identify the coupled plasmon modes to be originated from the interaction between two closely spaced tips with a narrow angular separation. Our analysis further estimates a range of angular separation between the tips that triggers the onset of the intertip coupling.

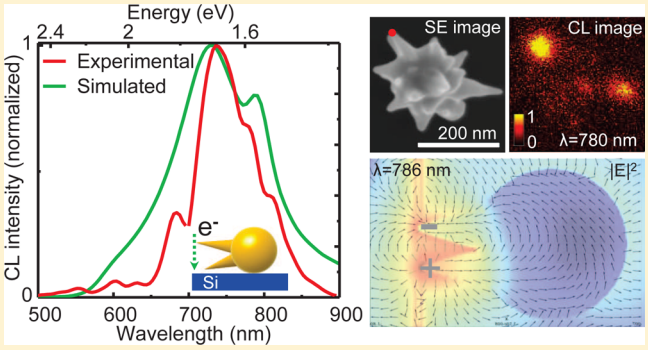

KEYWORDS: *cathodoluminescence, localized surface plasmon resonance, gold nanostar, electron beam spectroscopy, FDTD simulation*

Much attention has been paid in recent years to control and manipulate light[1,2] using noble metal nanoparticles (MNPs). The basic physical concept discussed[3] mostly in this connection is the idea of the so-called localized surface plasmons (LSPs), which are nonpropagating excitations of the conduction electrons in MNPs. LSP when excited resonantly[1−3] with a particular wavelength of the exciting light or evanescent wave associated with fast-moving electrons, shows considerable enhancement of the far-field intensity and similar enhancement of the near-field at the surface of the MNP, especially localized in the regions of sharp edges,[4−9] corners,[4−6] tips,[10−12] and apex, depending on the complexity of the morphology of the nanoparticles. The regions characterized by highly localized and strongly enhanced electromagnetic (EM) fields, known as plasmonic "hot spots",[12] are responsible for large enhancements in surface enhanced Raman scattering (SERS) signals[13] and have several interesting effects, such as enhanced fluorescence[14] or enhanced photocarrier generation,[15] that can have potential applications in biosensing, photovoltaics, and single molecule detection. In this context, multitipped (also called multipod, nanostar, or nanoflower) MNPs, especially, gold nanostars/nanoflowers are an exciting new class of plasmonic structures. Gold nanoflowers (AuNFs) consist of a near-spherical core from which numerous sharp tips of different lengths point outward. The significant tunability of the localized surface plasmon resonance (LSPR) wavelength over a wide range (from visible to NIR regime of the spectrum) and the corresponding strong electromagnetic (EM) field enhancement near apex of the tips have been utilized in many fields including detection and diagnosis of cancer affected cells,[16] plasmon enhanced microscopy such as surface-enhanced Raman scattering,[17−19] surface enhanced fluorescence,[20] photoelectron emission,[12] and photoluminescence[21] studies.

Tuning the frequency of the LSPR by varying the shape, size, and composition of MNPs as well as understanding the LSPR coupling of individual MNP with the other closely lying particles is a recent trend[22] in the area of plasmonics research. According to theoretical predictions,[10] each LSPR mode for single gold nanoflower (AuNF) is associated with one individual tip and the corresponding hotspot is located at the apex of tip assuming a wide separation among the tips so that tip to tip interaction can be neglected. Moreover, a tip to core plasmon coupling has also been invoked by the so-called plasmon hybridization model.[10] Most of the reported works on individual Au nanostar/nanoflower so far has demonstrated no tip to tip interaction.[10−12,19,23] This was primarily due to the large angular separation between the tips. However, if the number of tips in a single nanostar increases, angular separation between any two tips may be very small. In those cases, due to the random orientation of the tips protruding in three dimensions, tip−tip interaction cannot be neglected. Tip−tip interaction with the incident EM field may modify the spectral and spatial localization of the LSPR mode of the individual tips. This aspect, which has far reaching consequences in designing Au-NF morphology based SERS active substrate for maximizing the Raman signal, has not been addressed so far to the best of our knowledge. Consequently, experimental demonstration of

Received: August 22, 2014
Published: November 21, 2014

 © 2014 American Chemical Society

the modification of LSPR properties in spectral and spatial domain for closely lying tips of a single Au-NF is of utmost importance from the perspective of light matter interaction at the nanoscale.

Most of the studies for real-space imaging of plasmonic resonances of MNPs utilizing optical far-field techniques (excitation and detection in the far-field) are diffraction limited and thus a spatial resolution with a length scale below 200 nm is not easily achievable.[24] Other well-adapted techniques to probe LSPRs at the single NP level are photon scanning tunneling microscopy,[25] scanning near-field optical microscopy (SNOM),[26] and apertureless SNOM.[27] These techniques achieve better spatial resolution but often require fabrication of a very delicate probe in the form of a nanoscale sharp tip and may suffer from probe−sample interactions, distorting the signal of interest. An excellent alternative is electron microscopy based techniques, that is, electron energy loss spectroscopy (EELS)[4,6,28−30] and cathodoluminescence (CL) spectroscopy.[7,8,11,31−36] The high spatial resolution of about 1 nm or better for such techniques[4,6,37] is mainly governed by the ability of a modern scanning or transmission electron microscope (SEM or TEM) to focus an electron beam down to a diameter of 1 nm or below. The excitation mechanism of LSP modes with an electron beam is quite different from that of the optical excitation. An electron, or a beam of electrons, moving in vacuum can act as an evanescent source of supercontinuum light.[1] While a light source, as employed in dark-field microscopy (DFM),[23] excites the whole volume of the nanoparticle, a finely focused electron beam can act as a local probe to excite plasmons. CL is very closely related to the electromagnetic local density of states (EMLDOS) projected along the electron beam direction.[32,38,39] The working principle of CL-SEM is that energy is coupled from energetic electrons to the plasmon modes of the metallic nanostructure and subsequently to the propagating light modes that constitute one of the prominent decay channels for plasmons and causes enhancement in near field as well as the far-field intensity. Mapping the spatial variation of the photon emission is a direct probe of resonant modes of plasmonic nanostructures and, consequently, provides a direct way to map the local electric fields.

Here, we use CL-SEM technique to demonstrate the localization of electron beam excited plasmonic hotspots at the tips of individual AuNF. We present a detailed study of coupling between nearest neighbor tips originated from the same spherical core of the AuNF. The experimental CL spectra resulting from the electron beam impact near the apex of the closely spaced tips match well with the spectra calculated using finite difference time domain (FDTD) numerical method. The calculated electric near field intensity maps along with the associated vectorial plots of induced electric field show local enhancement of the field distribution in the apex and nearby region between the tips caused by the accumulation of charges of opposite signs at the neighboring tips. This confirms tip to tip or intertip coupling in a single gold multitipped nanoparticle, an aspect which has never been addressed before in the case of multitipped star/flower shaped gold nanoparticles. Furthermore, using 3D-FDTD simulations, we also show that a narrow angular separation between the nearest neighbor tips triggers the onset of intertip coupling.

RESULTS AND DISCUSSION

Observations under SEM reveal that the nanoparticles are often aggregated in clusters (SE image in Figure 1a). However, one

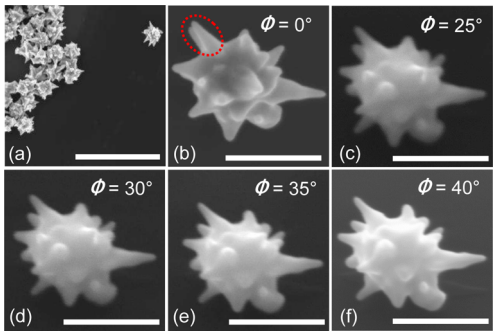

Figure 1. (a) SEM image of chemically synthesized gold nanoflowers in aggregates. (b) Selected isolated multitipped particle for the CL study. (c−f) Series of HRSEM images at different tilt angles, (ϕ, with respect to the incoming e-beam direction), confirm that two tips of nearly equal length encircled in (b) are aligned along out-of-plane direction with a narrow angular separation between them. The scale bar is 200 nm.

can also find sporadically spread isolated single multitipped gold nanoparticle. Representative SE image of such a single Au nanoparticle at high magnification is depicted in Figure 1b−f for different tilt angles (ϕ) of the sample stage (with respect to the impinging e-beam of the microscope) to aid clear visualization of the shape, size, and orientation of the adjacent tips with respect to one another. During CL study, the sample stage is restricted to be operated without tilt, and consequently, CL experiment was performed on this Au particle without tilt (SE image in Figure 1b). Morphologically, the single Au particle selected here (Figure 1b) is a multitipped spherical core from which the conical and petal shaped tips are protruding out in three directions, resembling like a flower, and hence, we will term this as gold nanoflower (AuNF) in the present study. In the following, we first collect the spectral data from tips marked as A, B, C, D, and E of the AuNF shown in the inset SE image of Figure 2a (the same as shown in Figure 1b) where the tips A (length and maximum diameter are 73 and 34 nm, respectively) and C are relatively longer (C being the largest tip of length 120 nm with a maximum diameter of 65 nm) than the tips B (length and maximum diameter are 46 and 35 nm, respectively), D (length and maximum diameter are 40 and 30 nm, respectively), and E (length and maximum diameter are 35 and 30 nm, respectively). Figure 2a shows CL spectra taken from apex regions of the above marked tips. The complete spectra were taken in two different wavelength ranges, 500−700 and 700−900 nm to make the sample not to be exposed under e-beam for longer time so that any adverse effect by e-beam induced drift on the spectral shift/distortion is minimized. The CL spectrum is strongest at the resonance peak wavelength near 736 nm in addition to the other resonance peaks around 670, 780, and 800 nm for the e-beam impact on the apex region of the tip A. The presence of resonance peaks, slightly blue-shifted from 670 nm, is common in the CL spectrum arising for the e-beam impact at the tips B, D, and E. On the other hand, the e-beam impact at the apex of tip C gives rise to two resonance peaks at around 860 and 590 nm. Moreover, a few weak peaks between 500 and 600 nm are also visible in all the spectra. To extract the spatial distribution

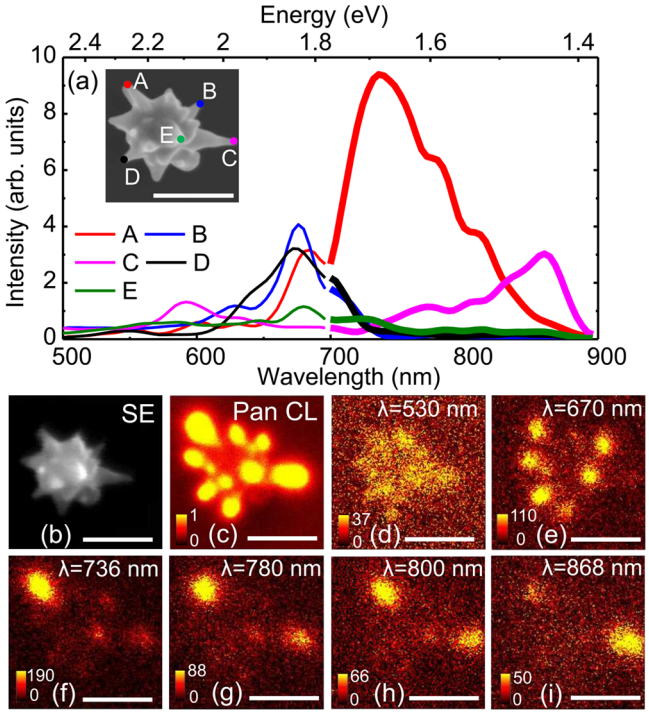

Figure 2. (a) Experimentally acquired CL spectra from different tip apex regions marked as A–E of the AuNF. The inset SEM image shows the e-beam impact points with different colored dots. (b) The SE image of the same AuNF and the corresponding (c) panchromatic CL image along with the monochromatic CL maps for the selected resonance wavelengths (d) 530, (e) 670, (f) 736, (g) 780, (h) 800, and (i) 868 nm. The scale bar is 200 nm.

of the photon emission, we acquired monochromatic CL maps at different peak wavelengths (Figure 2d–i), along with a panchromatic CL map (Figure 2c). Bright spots in the photon maps arise when the LSP modes are resonantly excited by the evanescent field associated with the electron beam. Intense luminescence is already discernible at the individual tips from the panchromatic photon map (Figure 2c). The monochromatic CL image obtained at 530 nm wavelength shows luminescent intensity when the electron beam scans over the core region (Figure 2d). Strong light emission occurs at other resonance wavelengths when the e-beam scans over the apex region of the tips. The LSPR at 530 nm is close to the plasmon mode of the spherical core.[10,11,30] The monochromatic photon maps of Figure 2d–i show that the luminescence enhancement of the AuNF is shifted to the far ends of the longer tips with the increase of the resonance wavelengths. This is consistent with the spectroscopic data presented in Figure 2a, as well as with our recent study.[11] The resonance wavelength of the tip plasmon mode depends strongly on the aspect ratio of the tip. The observation of the red-shift of the LSPR peaks with increasing tip length is well established both theoretically and experimentally.[10,11] Interestingly, while the photon maps corresponding to the CL peak wavelengths 736, 780, 800, and 868 nm (Figure 2f–i) indicate strong photon emission from individual longer tips of the AuNF, the CL map at 670 nm wavelength (Figure 2e) shows light emission from multiple tips, preferably of shorter length. This is expected as the CL spectra originating from the e-beam impact near the apex of shorter tips (namely, B, D, and E) are overlapped and peaked more or less near 670 nm. Moreover, the region of the spectrum beyond 670 nm is overlapped with the tail region of the strong resonance peak at 736 nm (originating from e-beam impact at tip A). Consequently, in the corresponding monochromatic map at 670 nm, we also see luminescence from tip A as well, while the e-beam scans near tip A. The resonance peaks associated with the longer tips correspond to the low-energy dipolar modes with plasmon oscillations confined around the tip regions.[23,40] The 670 nm peak is most probably due to the dipolar mode of oscillation of shorter tips, which are present in a large number near the core surface.[11] The general trend of our experimental finding is that, for all the shorter tips (B, D, and E), the major plasmon mode (dipolar) lies in the wavelength range 600–700 nm.

In passing, plasmonic response of a multibranched particle is dependent on the shape, size and number of the constituting branches/tips.[10,23] However, the orientation of the tips with respect to the substrate also plays a very crucial role on the plasmonic properties, as demonstrated quite recently by Das et al.[11] using FDTD-based numerical simulation for a model single tip Au nanostructure sitting on Si substrate. The study[11] showed reduction in the intensity and red shift of LSPR peaks, while the tip was moving from the parallel (w.r.t. the substrate) position toward the substrate maintaining the e-beam excitation on the tip apex. On the other hand, when the tip was moving away from the substrate, the observed blue-shift of the tip LSPR was attributed with uncoupling of the tip and the substrate (screened by the NP core). From the inset SE image of Figure 2a, it is clear that tips B, D, and E are oriented more or less away from the substrate as compared to the longer tips A and C. Consequently, LSP modes corresponding to these tips are blue-shifted w.r.t. the tips A and C modes. Also, tips B, D, and E being shorter tips with more or less similar lengths and diameter, their spectral peak positions lie approximately at the same wavelength of 670 nm. For the longest tip C, which is oriented more toward the substrate compared to the other tips studied here, both direct near-field absorption in the substrate and radiative emission into the substrate introduce a loss channel for the light confined in the particle. Consequently, one observes a broadening (i.e., damping) as well as reduced intensity in the corresponding emission spectrum at the resonance peak 868 nm (Figure 2a) for the electron beam excitation of the longest tip C. We discuss below about the tip mode A in detail.

The excitation of LSP caused by the e-beam impact at the apex region of tip A is of particular interest. Close inspection of the series of SEM images taken at different tilt angles (Figure 1b–f) clearly reveals that the tip A (encircled region of the SE image in Figure 1b) is not an isolated single tip, but is accompanied by an adjacent lower tip. While the upper tip in the encircled portion (in Figure 1b) is approximately parallel to the plane of substrate, the lower tip is slightly oriented toward the silicon substrate making an angular separation (θ) between the upper and the lower tip. It is also clear from the figures that the two tips are nearly equal in their lengths (~73 nm) and aspect ratio and originated from a spherical core of diameter ~ 160 nm. The close proximity of the apex of the upper tip with the lower one along the same vertical axis of the incoming electron beam thus makes it highly probable that the enhancement in the local field distribution as well as the far field radiation due to excitation of any one of these two tips being affected by that of the other tip. Consequently, one can expect coupling of the modes between such closely lying tips for e-beam impact near the region marked as A. In the following, we will focus on the origin of the strongest resonance

at 736 nm followed by the other small intensity peaks using FDTD numerical simulations. The numerical simulations were performed using the 3D-FDTD codes (commercially available from Lumerical Solutions). The details of the procedure have been described in the Methods section. We have modeled our AuNF structure as a spherical core having two conical tips (hereafter called the two-tip model, TTM), the geometrical configuration of which with respect to the Cartesian coordinate system is defined in Figure 3. The two closely spaced tips

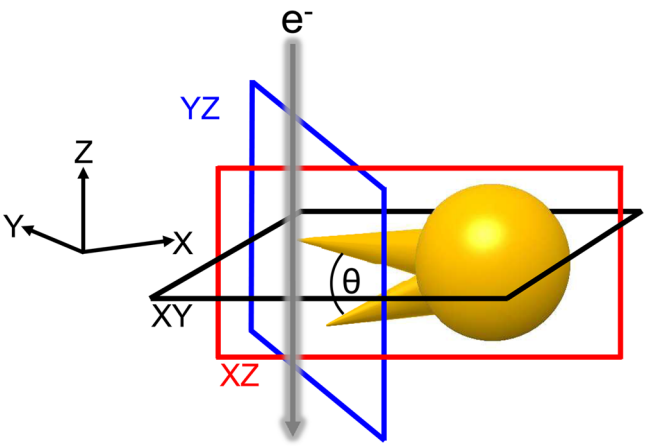

Figure 3. Schematic diagram of the geometrical configuration of the AuNF along with the coordinate system used in the numerical simulation. The star (two-tip model/TTM) is modeled as a spherical core with two tips. Incident electron beam is highlighted by the arrow. Power monitors were placed at the *XY*, *YZ*, and *XZ* planes in order to calculate the near field intensity and the charge distributions. The electron beam is kept in fixed position during all numerical calculations, unless mentioned specifically.

(length and aperture angle of the upper tip are 70 nm and 15° and that of lower tip are 70 nm and 14°) are assumed to be aligned in the *XZ* plane. During numerical simulation, the modeled e-beam is injected to the apex of the upper tip, as shown schematically in the inset of Figure 4a. The calculated emission spectrum (black curve in Figure 4a) with the resonance peaks at 733 and 786 nm matches reasonably well with the experimentally acquired CL spectrum (red curve in Figure 4a) having resonance peaks at 736 and 780 nm. It is also interesting to compare the emission spectra calculated with and without the Si substrate, as displayed in Figure 4b. The presence of the silicon substrate does not affect the LSPR peak positions (Figure 4b). However, the peak intensity is altered a bit. Hence, for numerical resource limitations, subsequent simulations are performed without the Si substrate unless mentioned specifically.

To understand further the effect of the individual upper and lower tip orientation separately on the spectrum, the spectrum was calculated assuming a single tip model (STM). The individual spectrum calculated for the e-beam impact on upper tip only shows LSPR at 744 nm, whereas for the e-beam impact on lower tip only shows resonance at 754 nm. Interestingly, the intensity for the upper tip is ∼1.3 times higher than the lower one as shown in Figure 4c. The decrease in intensity for the lower tip of nearly same dimension as the upper one can be accounted as follows: the evanescent field associated with the e-beam decays inversely with the distance from the e-beam trajectory at large distance from the beam. As a result, the strength of interaction with the e-beam is stronger for the upper

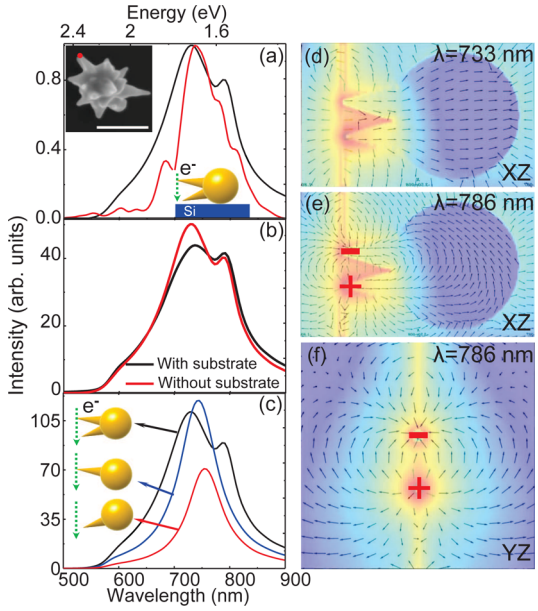

Figure 4. (a) Normalized numerically calculated (3D-FDTD) spectrum (black curve) of the TTM structure and experimentally acquired CL spectrum (red curve) in the wavelength range 500−700 nm. Inset SEM image shows the e-beam is focused at the red colored position. (b) Difference between the calculated spectra of the TTM structure, with substrate (black curve) and without substrate (red curve). The spectra are calculated in the 500−900 nm range. (c) Simulated emission spectrum of different structures. The black curve represents the TTM structure. The blue and red curves represent the spectrum of the single tip model/STM structure for upper and lower tip, respectively. Simulated near-field intensity ($|E|^2$) maps and the corresponding field maps at (d) 733 nm wavelength in the *XZ* plane, (e) 786 nm wavelength in the *XZ* plane, and (f) 786 nm wavelength in the *YZ* plane for TTM structure.

tip than the lower tip due to the larger separation of the lower tip apex and the incident e-beam. This decreases the intensity of the resonance peak in the calculated emission spectra for the excitation of the lower tip as compared to the upper tip in the STM structure (Figure 4c). The small shift in the LSPR positions (∼10 nm) can be due to the slight difference in the maximum diameter of the two tips. Moreover the finite mesh size used in FDTD simulations may also contribute to this small shift of 10 nm. Apart from this small shift in the calculated spectrum, the two resonance peaks for two individual tips at 744 and 754 nm seem to have the same type of plasmon mode, which is longitudinal dipolar in nature (shown in the figures in the Supporting Information). However, when the simulation is performed in the presence of two tips (in TTM structure), this longitudinal plasmon mode is split into two separate new plasmon modes at 733 and 786 nm, as displayed in Figure 4c (black curve). The peak at 733 nm was blue-shifted and the peak at 786 nm was red-shifted with respect to the longitudinal mode at 744/754 nm calculated for the individual tips (in STM structure). This indicates that, whenever we have two closely lying tips of nearly equal dimension, we have a coupling between their plasmon modes. In order to calculate the near electric field intensity ($|E|^2$) map and the corresponding mode of the surface plasmon oscillation (by plotting electric field vector map) at various resonant peak positions, we have placed field monitors at different planes in the TTM structure neglecting the silicon substrate, as shown in Figure 3. Now, from the simulated near field intensity maps of Figure 4e, we

see strong localization of the field near the apex as well as in-between the upper and lower tip at the 786 nm wavelength, indicating the existence of very large surface charge on the tip at this wavelength. Indeed, the associated vector plots (in the *XZ* plane) corresponding to this field intensity map show a clear dipole type field distribution where the accumulation of opposite charges is seen at the apex of the two tips. However, such tip to tip dipole formation is not observed in the vector plots (in the *XZ* plane) at the resonance wavelength 733 nm (Figure 4d). Moreover, the uniform field distribution as seen in the calculated vector plots (Figure 4d) on the surface of the core at 733 nm is highly disturbed (Figure 4e) by the strong tip to tip transverse dipole field lines as well as by the field lines of the longitudinal plasmon of the individual tip interacting with the core. That the tip−tip interaction is very strong at the resonance wavelength 786 nm is clear from the calculated near field intensity map and its associated vector plots drawn also in the *YZ* plane (Figure 4f) as well.

Thus, comparing the near field intensity maps along with the associated vector plots for the peak wavelengths 733 and 786 nm, the core-tip and tip−tip plasmonic modes of the AuNFs appears to be strongly coupled. Moreover, we have also verified using FDTD simulation that the coupling becomes more prominent when the adjacent tips are nearly equal in size. So, we presume the peak at 786 nm as seen in the experimental CL spectra of Figure 2g is a coupled LSP mode originating due to the strong electrostatic interaction between the two closely spaced out-of-plane tips of an AuNF where the oscillating dipole is aligned along the out of plane direction either in *XZ* or *YZ* planes, as shown in Figure 4e,f. That such strong coupling of the LSPR mode leads to significant near-field enhancement, as observed here, is also accompanied by an increased nonradiative LSPR damping,[21] which is the reason why we see strongest intensity at the resonance around 736 nm (longitudinal dipole mode) observed in the present experiment. Although the coupling of the LSPRs between the two closely lying separate particles has been studied to some extent in recent years,[22] the evidence of the coupling within the two closely lying branches of a same nanoparticle as in the AuNF of the present study has not been reported so far to the best of our knowledge. However, we should mention here that while the experimentally acquired CL spectrum (Figure 4a) has four resonance peaks, the FDTD spectrum exhibits two resonance peaks. The difference can be attributed mainly to the modeling with single- or two-tipped core compared to the actual core with numerous tips employed in the experiment. Moreover, the uncertainty in the exact shape/orientations of the tips of the nanoflower obtained from SEM imaging on the basis of which we modeled the structure may also contribute to the observed difference between experiment and theory. The other reasons for the deviation may include the uncertainty in the exact location of the e-beam due to small drift of the specimen during spectrum acquisition, and the possibility of the presence of CTAB surfactant layer between the particle and the substrate causing a change of dielectric environment not considered in the simulation.

Now, for deeper insight of the out of plane tip−tip interaction, the lower tip has been rotated in anticlockwise direction keeping the upper tip at the same position (Figure 5). It is noted that with increasing angular separation (θ), the tip to tip interaction mode shows a blue shift. At lower angles less than $\theta + 10°$ when the tip apex are very close to each other, the induced charges near the apex of the tips can interact very

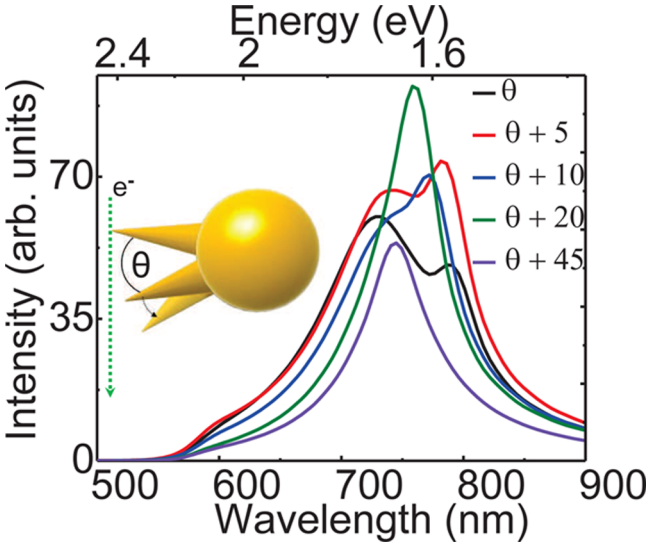

Figure 5. Intertip coupling and resonance splitting in two-tip model/TTM structure as a function of the angular separations $\theta + 5°$, $\theta + 10°$, $\theta + 20°$, $\theta + 45°$ respectively between two closely lying tips where θ is the initial angle between the tips. The electron beam was kept in fixed position similar to the previous simulations.

strongly via electrostatic interaction requiring less energy. However, when the tip to tip distance is large at higher angular separation, obviously the tip−tip interaction requires more energy to compete the tip-core interaction. Consequently, coupled mode associated with the tip−tip interaction is shifted toward the high energy or shorter wavelength regime. From the spectra shown in Figure 5, it is also clear that the splitting of the resonance peak as per TTM structure disappears gradually and turns into one LSP mode for very large angular separation. This single LSP mode is probably a mixing/combination of tip−tip coupled mode and core-tip longitudinal mode. Observation of such mode mixing is possible only by using the electron beam as an excitation source, which can excite the longitudinal as well as the transverse plasmon mode at the same instant for its evanescent nature. At an angle greater than ($\theta + 45°$), when the lower tip is far away from the upper tip, coupling between two tips becomes negligible. Additionally, the tip-core longitudinal plasmon mode for the lower tip also becomes less prominent due to the larger separation between the lower tip and the electron beam position. Consequently, the two-tip model (TTM) will behave like the single tip model (STM) for upper tip showing only a single resonance peak at 744 nm (violet curve in Figure 5), similar to the spectrum of the single tip model applied for upper tip, as shown in Figure 4c (blue curve).

■ CONCLUSIONS

In summary, site-specific cathodoluminescence (CL) spectroscopy and imaging technique in a high-resolution scanning electron microscope (HRSEM) have been used to investigate different localized surface plasmon (LSP) modes associated with the widely separated individual tips as well as closely lying tips of single gold nanoflower (AuNF) on a silicon substrate both in the spatial and in the spectral domain. The combination of CL-SEM technique and FDTD simulation have helped us to identify for the first time the plasmonic coupling between two nearest-neighbor out-of-plane tips protruded from the same spherical core. Detailed analysis shows that such intertip coupling within the same nanoparticle is effective within a

narrow angular separation between the closely lying tips and is the origin of the double-peaked strong resonance mode observed in the single AuNF of the present study. The simulated near field intensity maps drawn at the coupled LSPR mode show strong local field enhancement near the apex as well as in-between the closely lying upper and lower tip. This has far reaching consequences in designing Au nanostar morphology based SERS active substrate for maximizing the Raman signal. Consequently, the present study is important to understand the mechanism of local electron probe driven plasmonic interaction within different branches/tips of a single 3-D complex nanostructure that might have far reaching consequences in applications where localized electromagnetic field enhancement is exploited for maximizing the light signal, such as in surface-enhanced Raman scattering based spectroscopy, biosensing, or designing nanoparticle embedded solar cells.

METHODS

Chemical Synthesis of Gold Nanoflower. *Chemicals.* Chemicals including gold(III) chloride trihydrate ($HAuCl_4 \cdot 3H_2O$) ≥99.9% trace metal basis, silver nitrate ($AgNO_3$) BioXtra ≥99% (titration), sodium borohydride (H_4BNa) granular, 10−40 mesh 98%, L-ascorbic acid ($C_6H_8O_6$) ACS reagent ≥99%, and hexadecyltrimethylammonium bromide or CTAB ($C_{19}H_{42}BrN$) assay ≥99% (AT) were purchased from Sigma-Aldrich (Germany) and used for the synthesis without any further purification. All the synthesis and experimental works have been done by using Milli-Q water.

Synthesis of Gold Nanoseed. Gold nanoflowers (GNFs) are synthesized by using a multistep seeding-based nanotemplating method[41] where the final step seed is a nano template for predetermined tailored shape. In the first step, we synthesize spherical gold nanoseed by adding 0.5 mL of 10^{-2} M $HAuCl_4$ solution with 20 mL of water in a small vial. Next 0.2 mL of 2.5 × 10^{-2} M trisodium citrate solution was added dropwise and left for 1 min to mix well. After that, 60 μL of 10^{-1} M ice cold freshly prepared $NaBH_4$ solution is added drop by drop, which changes the solution color from light yellow to light red. We keep this seed solution for another 2 h before using it for the next synthesis step. During this time, the color of the solution turns to deep red. Nano seeds exhibit absorption spectra with absorption maxima at 510 nm, which corresponds to 4.3 ± 1.4 nm seed, has been confirmed by TEM.

First Growth Step to Synthesize Gold Nano Popcorns (GNPops). In the first growth step, we have synthesized mono dispersed GNPops with average size of about 45 ± 3 nm. To synthesize GNPops, we dissolve 0.049 g of CTAB in 45 mL of water (2.8 × 10^{-3} M) by mild heating and simultaneous constant slow stirring. To this solution, 2 mL of 10^{-2} M $HAuCl_4$ solution is added and stirred for an additional 1 min. Then 300 μL of 10^{-2} M freshly prepared $AgNO_3$ solution is added gently and mixed well, and then 320 μL of 10^{-1} M ascorbic acid is added dropwise. As soon as the solution becomes colorless, 500 μL of gold nanoseed solution (as prepared) is added at a time. The solution becomes deep blue within a minute and is left still for 2 h before using it for the next synthesis step.

Nanotemplating Step to Synthesize GNFs. In the second growth step, we have synthesized intrinsically monodispersed GNFs with size (diameter) variation between 110 and 360 nm. To synthesize different sized GNFs with differential petal openings, we used 11 different growth solutions by dissolving 0.005, 0.01, 0.025, 0.05, 0.1, 0.25, 0.5, 0.75, 1.0, 1.25, and 1.5 g of CTAB in 45 mL of water by mild heating and constant stirring. To this solution, 2 mL of 10^{-2} M $HAuCl_4$ solution was added and stirred for an additional 1 min. Then 300 μL of 10^{-2} M freshly prepared $AgNO_3$ solution was added gently and mixed well, and then 320 μL of 10^{-1} M ascorbic acid is added dropwise. As the solution becomes colorless, immediately 500 μL of GNPop solution was added at a time as nanotemplate, and the solution is left undisturbed for overnight to complete the growth process and different growth solutions show different bright color. The diluted AuNF solution is drop coated on a cleaned Si(100) wafer and then loaded into the SEM chamber after sufficient drying in ambient condition.

CL Spectroscopy and Imaging. CL spectroscopy and imaging have been performed using the Gatan MonoCL3 optical detection system attached with ZEISS SUPRA40 field emission gun (FEG) SEM.[42] The MonoCL3 system is equipped with a retractable paraboloid mirror placed inside the SEM chamber. The electron beam reaches the sample through a hole of 1 mm diameter on the paraboloid mirror. The mirror is capable of collecting emitted light signals from the sample under consideration within a solid angle of 1.42π sr of the full 2π of the upper half sphere. The collected light signal is collimated through a hollow aluminum tube and directed to a Czerny-Turner type optical monochromator of focal length of 300 mm. Finally, the signal from the monochromator is fed to a Peltier-cooled high sensitivity photomultiplier tube (HSPMT). In order to capture a maximum amount of light signal, the top surface of the sample must be kept at the focal plane of the paraboloid mirror. In our experimental arrangements, this is achieved by putting the sample top surface 1 mm below the bottom plane of the mirror. This focal adjustment is very carefully done before every set of experiments and the detailed procedure can be found elsewhere.[42] All the CL data in the present experiment are acquired with electron beam energy of 30 keV and beam current of ∼15 nA and the diameter of the beam spot is about 5 nm. The CL system can be operated in two modes, namely, monochromatic and panchromatic. In the monochromatic mode, the electron beam is either scanned over an area of interest or fixed onto a selected point of the sample. The photons emitted from the sample pass through the monochromator and enter the HSPMT detector and the recording of CL spectra is accomplished. Then monochromatic CL images or photon maps at selected peak wavelengths are obtained by scanning the electron beam over the sample while allowing only the light signal of desired wavelength to pass through the monochromator to the HSPMT. In the panchromatic mode, the monochromator is bypassed and the emitted light is directly fed to the HSPMT detector. The panchromatic photon map is obtained by scanning the e-beam over the sample resulting in a CL emission map that contains all the wavelengths lying within the detection range (300−900 nm) of the HSPMT. Spectral step size and dwell time were kept fixed at 4 nm and 0.25 s, respectively, during the entire experiment. The monochromatic CL images are recorded with 150 × 150 pixels and the total exposure time in capturing one frame is 11.25 s. Both the monochromatic and panchromatic mode of CL operation also allow us simultaneous acquisition of secondary electron (SE) images enabling direct correlation between plasmonic response and the particle morphology.

FDTD Simulations for Electron Beam Excitation. We have used 3D-FDTD (commercially available FDTD package from the Lumerical Solutions, version 8.4) numerical simulation for a

detailed analysis of the surface plasmon assisted photon emission. In our numerical calculations, we have simulated the electron beam as the source of EM excitation. In our CL experiments, we have used electron beam energy of 30 keV and beam current of 15 nA. This means the electron impact to the sample on an average in every 11 ps, which is ∼5000 times longer than one typical optical cycle in the visible spectral range and ∼200 times longer than the typical electron relaxation time in gold. So, we can neglect the electron−electron interaction and simulate the photon emission for one single electron impact. In this numerical procedure we have modeled the energetic electron as a large number of closely spaced dipoles placed vertically with a temporal phase lag that is associated with the electron velocity. The current density can be written as

$$J(t, \vec{r}) = -ev\hat{u}_z\delta(z - vt)\delta(x - x_0)\delta(y - y_0) \quad (1)$$

where e is the electronic charge and v is the velocity of electron, (x_0,y_0) represents the position of the electron beam, and z is the direction of electron velocity and $\hat{u}_z$ is the unit vector along the z direction. The introduced phase lag factor between two consecutive dipole is (z/v), where $v = 0.32c$ corresponding to the 30 keV electron energy used in the present experiment, with c being the velocity of light in free space. In the absence of any structure, the e-beam will not generate any radiation because it is moving at a constant velocity. But in FDTD, we are obliged to simulate only a finite portion of the electron beam path, and the sudden appearance and disappearance of the dipole beam will induce radiation. To minimize error arising due to this issue, we run a second reference simulation where all the structures have been removed, and we can calculate the electromagnetic fields at angular frequency ω by taking the difference in fields between the simulations. The CL emission spectra are calculated by integrating the Poynting vector components (P_z) normal to a large arbitrary surface in the upper hemisphere. This is realized in simulations by placing a very large XY plane 500 nm above the top surface of the nanoparticle. In order to calculate the near field intensity $(|E|^2)$ map and the charge distribution map corresponding to the calculated CL emission spectra, we have placed the field monitors at suitable planes passing through or very near to the nanoflower. The dispersive property of gold in the wavelength range 500−900 nm has been taken from the tabulated value of Johnson and Christy.[43] The Si substrate is considered as a nondispersive material with fixed refractive index 4 in the same wavelength range and having a dimension of 5 μm × 5 μm × 4 μm. The metallic structures having resonant characteristics and high index contrast interfaces are critically sensitive to the precise locations of material interfaces. So, for a better accuracy in all the calculations, we have used the Lumerical's mesh override region over all the metallic structure. The size of fine mesh cells near the metallic structure was kept in the same value during all the numerical simulations and it was 2 nm × 2 nm × 2 nm.

■ ASSOCIATED CONTENT

Supporting Information

Field distributions and vector maps for individual single tip models (STMs). This material is available free of charge via the Internet at http://pubs.acs.org.

■ AUTHOR INFORMATION

Corresponding Author

*E-mail: tapask.chini@saha.ac.in. Fax: +91 33 2337 4637.

Present Address

†Laboratoire de Physique des Solides, CNRS UMR8502, Univ. Paris Sud, 91405 Orsay, France. This work was carried out when the author was in Saha Institute of Nuclear Physics.

Notes

The authors declare no competing financial interest.

■ ACKNOWLEDGMENTS

We are grateful to the Department of Atomic Energy (DAE), Government of India, for the financial support.

■ REFERENCES

(1) García de Abajo, F. J. Optical excitations in electron microscopy. *Rev. Mod. Phys.* **2010**, *82*, 209−275.

(2) Giannini, V.; Fernández-Domínguez, A. I.; Heck, S. C.; Maier, S. A. Plasmonic nanoantennas: fundamentals and their use in controlling the radiative properties of nanoemitters. *Chem. Rev.* **2011**, *111*, 3888−3912.

(3) Maier, S. A. *Plasmonics: Fundamentals and Applications*; Springer: New York, 2007.

(4) Myroshnychenko, V.; Nelayah, J.; Adamo, G.; Geuquet, N.; Rodríguez-Fernández, J.; Pastoriza-Santos, I.; MacDonald, K. F.; Henrard, L.; Liz-Marzán, L. M.; Zheludev, N. I.; Kociak, M.; García de Abajo, F. J. Plasmon spectroscopy and imaging of individual gold nanodecahedra: a combined optical microscopy, cathodoluminescence, and electron energy-loss spectroscopy study. *Nano Lett.* **2012**, *12*, 4172−4180.

(5) Angulo, A. M.; Noguez, C.; Schatz, G. C. Electromagnetic field enhancement for wedge-shaped metal nanostructures. *J. Phys. Chem. Lett.* **2011**, *2*, 1978−1983.

(6) Nelayah, J.; Kociak, M.; Stéphan, O.; García de Abajo, F. J.; Tencé, M.; Henrard, L.; Taverna, D.; Pastoriza-Santos, I.; Liz-Marzán, L. M.; Colliex, C. Mapping surface plasmons on a single metallic nanoparticle. *Nat. Phys.* **2007**, *3*, 348−353.

(7) Das, P.; Chini, T. K.; Pond, J. Probing higher order surface plasmon modes on individual truncated tetrahedral gold nanoparticle using cathodoluminescence imaging and spectroscopy combined with FDTD simulations. *J. Phys. Chem. C* **2012**, *116*, 15610−15619.

(8) Das, P.; Chini, T. K. Spectroscopy and imaging of plasmonic modes over a single decahedron gold nanoparticle: a combined experimental and numerical study. *J. Phys. Chem. C* **2012**, *116*, 25969−25976.

(9) Willets, K. A. Probing local electromagnetic field enhancements on the surface of plasmonic nanoparticles. *Prog. Surf. Sci.* **2012**, *87*, 209−220.

(10) Hao, F.; Nehl, C. L.; Hafner, J. H.; Nordlander, P. Plasmon resonances of a gold nanostar. *Nano Lett.* **2007**, *7*, 729−732.

(11) Das, P.; Kedia, A.; Kumar, P. S.; Large, N.; Chini, T. K. Local electron beam excitation and substrate effect on the plasmonic response of single gold nanostars. *Nanotechnology* **2013**, *24*, 405704.

(12) Hrelescu, C.; Sau, T. K.; Rogach, A. L.; Jäckel, F.; Laurent, G.; Douillard, L.; Charra, F. Selective excitation of individual plasmonic hotspots at the tips of single gold nanostars. *Nano Lett.* **2011**, *11*, 402−407.

(13) Alonso-González, P.; Albella, P.; Schnell, M.; Chen, J.; Huth, F.; Gracía-Etxarri, A.; Casanova, F.; Golmar, F.; Arzubiaga, L.; Hueso, L. E.; Aizpurua, J.; Hillenbrand, R. Resolving the electromagnetic mechanism of surface-enhanced light scattering at single hot spots. *Nat. Commun.* **2012**, *3*, 684.

(14) Wang, Y.; Yang, T.; Tuominen, M. T.; Achermann, M. Radiative rate enhancements in ensembles of hybrid metal-semiconductor nanostructures. *Phys. Rev. Lett.* **2009**, *102*, 163001.

(15) Atwater, H. A.; Polman, A. Plasmonics for improved photovoltaic devices. *Nat. Mater.* **2010**, *9*, 205−213.

(16) Lu, W.; Singh, A. K.; Khan, S. A.; Senapati, D.; Yu, H.; Ray, P. C. Gold nano-popcorn-based targeted diagnosis, nanotherapy treatment, and in situ monitoring of photothermal therapy response of prostate cancer cells using surface-enhanced Raman spectroscopy. *J. Am. Chem. Soc.* **2010**, *132*, 18103−18114.
(17) Chirumamilla, M.; Toma, A.; Gopalakrishnan, A.; Das, G.; Zaccaria, R. P.; Krahne, R.; Rondanina, E.; Leoncini, M.; Liberale, C.; De Angelis, F.; Di Fabrizio, E. 3D nanostar dimers with a sub-10-nm gap for single-/few-molecule surface-enhanced Raman scattering. *Adv. Mater.* **2014**, *26*, 2353−2358.
(18) Khoury, C. G.; Vo-Dinh, T. Gold nanostars for surface-enhanced Raman scattering: synthesis, characterization and optimization. *J. Phys. Chem. C* **2008**, *112*, 18849−18859.
(19) Aldeanueva-Potel, P.; Carbó-Argibay, E.; Pazos-Pérez, N.; Barbosa, S.; Pastoriza-Santos, I.; Alvarez-Puebla, R. A.; Liz-Marzán, L. M. Spiked gold beads as substrates for single-particle SERS. *ChemPhysChem* **2012**, *13*, 2561−2565.
(20) Le Ru, E. C.; Etchegoin, P. G.; Grand, J.; Félidj, N.; Aubard, J.; Lévi, G. Mechanisms of spectral profile modification in surface-enhanced fluorescence. *J. Phys. Chem. C* **2007**, *111*, 16076−16079.
(21) Zhang, T.; Lu, G.; Shen, H.; Shi, K.; Jiang, Y.; Xu, D.; Gong, Q. Photoluminescence of a single complex plasmonic nanoparticle. *Sci. Rep.* **2014**, *4*.
(22) Halas, N. J.; Lal, S.; Chang, W.-S.; Link, S.; Nordlander, P. Plasmons in strongly coupled metallic nanostructures. *Chem. Rev.* **2011**, *111*, 3913−3961.
(23) Shao, L.; Susha, A. S.; Cheung, L. S.; Sau, T. K.; Rogach, A. L.; Wang, J. Plasmonic properties of single multispiked gold nanostars: correlating modeling with experiments. *Langmuir* **2012**, *28*, 8979−8984.
(24) Ghenuche, P.; Cherukulappurath, S.; Taminiau, T. H.; van Hulst, N. F.; Quidant, R. Spectroscopic mode mapping of resonant plasmon nanoantennas. *Phys. Rev. Lett.* **2008**, *101*, 116805.
(25) Sandtke, M.; Kuipers, L. Slow guided surface plasmons at telecom frequencies. *Nat. Photonics* **2007**, *1*, 573−576.
(26) Bakker, R. M.; Boltasseva, A.; Liu, Z.; Pedersen, R. H.; Gresillon, S.; Kildishev, A. V.; Drachev, V. P.; Shalaev, V. M. Near-field excitation of nanoantenna resonance. *Opt. Express* **2007**, *15*, 13682−13688.
(27) Rang, M.; Jones, A. C.; Zhou, F.; Li, Z.-Y.; Wiley, B. J.; Xia, Y.; Raschke, M. B. Optical near-field mapping of plasmonic nanoprisms. *Nano Lett.* **2008**, *8*, 3357−3363.
(28) Bosman, M.; Ye, E.; Tan, S. F.; Nijhuis, C. A.; Yang, J. K. W.; Marty, R.; Mlayah, A.; Arbouet, A.; Girard, C.; Han, M.-Y. Surface plasmon damping quantified with an electron nanoprobe. *Sci. Rep.* **2013**, *3*.
(29) Koh, A. L.; Bao, K.; Khan, I.; Smith, W. E.; Kothleitner, G.; Nordlander, P.; Maier, S. A.; McComb, D. W. Electron energy-loss spectroscopy (EELS) of surface plasmons in single silver nanoparticles and dimers: influence of beam damage and mapping of dark modes. *ACS Nano* **2009**, *3*, 3015−3022.
(30) Mazzucco, S.; Stéphan, O.; Colliex, C.; Pastoriza-Santos, I.; Liz-Marzan, L. M.; Garcia de Abajo, J.; Kociak, M. Spatially resolved measurements of plasmonic eigenstates in complex-shaped, asymmetric nanoparticles: gold nanostars. *Eur. Phys. J.: Appl. Phys.* **2011**, *54*, 33512.
(31) Yamamoto, N.; Araya, K.; García de Abajo, F. J. Photon emission from silver particles induced by a high-energy electron beam. *Phys. Rev. B* **2001**, *64*, 205419.
(32) Kuttge, M.; Vesseur, E. J. R.; Koenderink, A. F.; Lezec, H. J.; Atwater, H. A.; García de Abajo, F. J.; Polman, A. Local density of states, spectrum, and far-field interference of surface plasmon polaritons probed by cathodoluminescence. *Phys. Rev. B* **2009**, *79*, 113405.
(33) Vesseur, E. J. R.; de Waele, R.; Kuttge, M.; Polman, A. Direct observation of plasmonic modes in Au nanowires using high-resolution cathodoluminescence spectroscopy. *Nano Lett.* **2007**, *7*, 2843−2846.
(34) Gómez-Medina, R.; Yamamoto, N.; Nakano, M.; García de Abajo, F. Mapping plasmons in nanoantennas via cathodoluminescence. *New J. Phys.* **2008**, *10*, 105009.
(35) Denisyuk, A. I.; Adamo, G.; MacDonald, K. F.; Edgar, J.; Arnold, M. D.; Myroshnychenko, V.; Ford, M. J.; García de Abajo, F. J.; Zheludev, N. I. Transmitting Hertzian optical nanoantenna with free-electron feed. *Nano Lett.* **2010**, *10*, 3250−3252.
(36) Das, P.; Chini, T. K. Substrate induced symmetry breaking in penta-twinned gold nanorod probed by free electron impact. *J. Phys. Chem. C* **2014**, *118*, 26284−26291.
(37) Knight, M. W.; Liu, L.; Wang, Y.; Brown, L.; Mukherjee, S.; King, N. S.; Everitt, H. O.; Nordlander, P.; Halas, N. J. Aluminum plasmonic nanoantennas. *Nano Lett.* **2012**, *12*, 6000−6004.
(38) Kociak, M.; Stéphan, O. Mapping plasmons at the nanometer scale in an electron microscope. *Chem. Soc. Rev.* **2014**, *43*, 3865−3883.
(39) Barnard, E. S.; Coenen, T.; Vesseur, E. J. R.; Polman, A.; Brongersma, M. L. Imaging the hidden modes of ultrathin plasmonic strip antennas by cathodoluminescence. *Nano Lett.* **2011**, *11*, 4265−4269.
(40) Kumar, P. S.; Pastoriza-Santos, I.; Rodríguez-González, B.; García de Abajo, F. J.; Liz-Marzán, L. M. High-yield synthesis and optical response of gold nanostars. *Nanotechnology* **2008**, *19*, 015606.
(41) Bardhan, M.; Satpati, B.; Ghosh, T.; Senapati, D. Synergistically controlled nano-templated growth of tunable gold bud-to-blossom nanostructures: A pragmatic growth mechanism. *J. Mater. Chem. C* **2014**, *2*, 3795−3804.
(42) Das, P.; Chini, T. K. An advanced cathodoluminescence facility in a high-resolution scanning electron microscope for nanostructure characterization. *Curr. Sci.* **2011**, *101*, 849−854.
(43) Johnson, P. B.; Christy, R. W. Optical constants of the noble metals. *Phys. Rev. B* **1972**, *6*, 4370.